

# Hayabusa2 Surface and Shock Layer Radiation from the Australian Airborne Observation

Ranjith Ravichandran\*, Byrenn Birch<sup>†</sup>, Andrew Lock<sup>‡</sup>, David Buttsworth<sup>§</sup> and Fabian Zander<sup>¶</sup>  
*University of Southern Queensland, Toowoomba, Queensland 4350, Australia.*

Characterization of the radiating flowfield around a spacecraft during its atmospheric entry is of significant value for heat shield design. The reentry of the Hayabusa2 sample return capsule (SRC) was observed from an airborne platform by the Australian Airborne Observation team. This paper reports the extended analysis performed on Hayabusa2 spectral data by converting the data to spectral radiance and emission coefficient, given that the trajectory data of the SRC at each observation point is now available. Attenuation due to atmospheric effects has been accounted for in this analysis with a calculated atmospheric transmission at each trajectory point in time. Surface temperature and its spatial distribution were determined by Planck curve fitting and an empirical temperature distribution model. Surface temperatures varied from 2500 K to 3700 K during the measurement. Spectral emission coefficients of atomic lines were calculated taking into account a region of shock layer volume where gas temperature would exceed 7000 K. Presenting the atmospheric transmission corrected observation data in spectral radiance and emission coefficient terms eliminates the dependence on observer's location for a given view angle enabling direct comparison with numerical flowfield radiation results.

## Nomenclature

$A$	=	surface area, $\text{m}^2$
$c$	=	speed of light in vacuum, $2.9979 \times 10^8 \text{ m s}^{-1}$
$d$	=	distance from the observer to emitting source, m
$\Delta l$	=	capsule distance segment in a given atmospheric layer, m
$\Delta z$	=	thickness of a given atmospheric layer, m
$E$	=	spectral irradiance, $\text{W m}^{-2} \text{ nm}^{-1}$
$h$	=	Planck constant, $6.6261 \times 10^{-34} \text{ J s}$

---

\*Postdoctoral Research Fellow, Institute of Advanced Engineering and Space Sciences; ranjith.ravichandran@unisq.edu.au.

<sup>†</sup>Senior Lecturer, School of Engineering. Member AIAA.

<sup>‡</sup>Postdoctoral Research Fellow, Institute of Advanced Engineering and Space Sciences.

<sup>§</sup>Professor, School of Engineering. Member AIAA.

<sup>¶</sup>Associate Professor, School of Engineering. Member AIAA.

$j$	=	spectral emission coefficient, $\text{W m}^{-3} \text{sr}^{-1} \text{nm}^{-1}$
$k$	=	Boltzmann constant, $1.3806 \times 10^{-23} \text{J K}^{-1}$
$L$	=	spectral radiance, $\text{W m}^{-2} \text{sr}^{-1} \text{nm}^{-1}$
$n$	=	number density, $\text{cm}^{-3}$
$T$	=	temperature, K
$\varepsilon$	=	surface emissivity, –
$\lambda$	=	wavelength, m
$\sigma$	=	absorption cross-section, $\text{cm}^2$
$\tau$	=	optical depth, –
$\delta$	=	equivalent depth of shock layer, m
$\mathcal{T}$	=	atmospheric transmission, –
$\theta$	=	zenith angle, $^\circ$
$\phi$	=	view angle, $^\circ$
$\alpha$	=	elevation angle, $^\circ$
$\gamma$	=	azimuth angle, $^\circ$
$\Omega$	=	solid angle, sr

*Subscripts*

app	=	apparent
obj	=	parameters referring to target reentry object (Hayabusa2 SRC)
peak	=	peak value
SL	=	shock layer
vertical	=	corresponds to vertically viewing scenario
$\alpha$	=	denotes first spectral line in Balmer series (atomic Hydrogen emission lines)
$\lambda$	=	denotes parameters that vary with wavelength

## I. Introduction

**S**AMPLE return capsules (SRC) reenter into the atmosphere of Earth to safely return the samples collected from distant comets/asteroids. Other hypervelocity reentry events include the atmospheric entry of celestial objects such as meteoroids (resulting in meteors or even meteor showers), and man-made objects categorized as space debris. Due to very high entry speeds, up to  $12 \text{ km s}^{-1}$ , the spacecraft is exposed to extreme heating loads as a shock layer forms in front of it. The gas species inside the shock layer will undergo dissociation and ionization processes, and chemical reactions take place among the gas species and the species from the heat shield material. This results in a highly

non-equilibrium thermochemical scenario with electromagnetic radiation emitting from various species formed during the reactions; including dissociated, recombined gas species, and newly formed ablation byproducts. Atmospheric entry of space capsules, space debris, and meteor showers are excellent opportunities to observe and record the radiation emitted from the aerodynamically heated shock layer formed in front of the reentering object and the thermal radiation from the hot surface of the reentry body. Characterization of the radiating flowfield is very valuable in understanding the aerothermodynamics of reentry. Conventionally these radiating flowfields have been experimentally simulated and tested in ground testing facilities. Ground testing facilities of various types, such as shock/expansion tunnels and plasma wind tunnels, have limited capability in that they can reproduce only certain aspects of the flow but not the complete reentry conditions.

Flight observations of such rare reentry events, both ground-based and airborne, are advantageous and serve as a validation data for numerical simulations. Previous observation campaigns such as Stardust [1], Genesis [2], ATV-1 [3], Hayabusa [4–7], Cygnus OA6 (resupply spacecraft to ISS operated by Orbital ATK) [8], WT1190F [9], and meteor showers such as Draconids [10] and Tau-Herculids [11] prove to be very valuable in studying the reentry scenarios. Compared to ground-based platforms, airborne platforms provide the advantage of recording emission data with a minimized effect of atmospheric attenuation of radiation. The Hypersonics and Rocketry group at the University of Southern Queensland, Australia have actively participated in and led several observation campaigns with international collaborations including airborne and ground-based observations. The tracking data recorded from such missions have resulted in estimating the capsule's trajectory independently [12]. In addition, spectral emission data have also been analyzed to identify the emitting atomic species and study the time history of surface temperature and irradiance [4, 13, 14].

The Hayabusa2 sample return capsule was separated from its mother spacecraft about 12 hours prior to the reentry event. It reentered into Earth's atmosphere at a velocity of  $12 \text{ km s}^{-1}$  directly from the interplanetary transfer orbit [15], safely returning asteroid samples in a container. On the 5<sup>th</sup> of December 2020, at approximately 17:29:00 Coordinated Universal Time (UTC), the SRC from the Hayabusa2 spacecraft was visible to airborne observers over the Woomera desert in Australia. The Australian Airborne Observation team from the University of Southern Queensland and the University of Queensland observed the reentering Hayabusa2 SRC along with other international research teams [13, 15–24]. Measurements were taken by the Australian team using 11 transmission grating spectrographs (visible/near-infrared), an infrared camera, and a Sony A7iiiR camera for regular video [16]. The observed data has been analyzed in spectral irradiance units and further used to estimate the apparent surface temperatures [13]. Similar approaches of surface temperature estimation have been used previously for reentry observation data [4, 22]. Surface temperatures have also been predicted using computational tools [19]. Birch et al. further extended the analysis using a parameterized empirical model to identify spatial distribution of surface temperature [14].

This paper extends the analysis to convert data into units of spectral radiance and emission coefficients (for atomic line

emission) to characterize the radiation from the reentry flowfield and to determine the surface temperature distribution. Knowledge of the reentering object's position along the trajectory is essential to process the observed spectral data and thus quantify the object's absolute radiation signatures. The view angle of the capsule and its distance away from the observer can only be calculated if the instantaneous locations of the capsule and the observer are known. Spectral irradiance at the observer's location can be used when the absolute spectral radiance is not of interest, and the qualitative shape of the spectra would suffice to investigate the problem; for example Planck curve fitting of the spectral data to estimate a surface temperature. Conventionally, the radiation data from observation campaigns are presented in calibrated spectral irradiance units as received at the observer's location [25], or at a hypothetical distance of 100 km from the capsule [4]. Converting the Hayabusa2 re-entry data into emission coefficient terms is very valuable in understanding the radiating flowfield, as well as serve as a validation data for numerical modeling as it uniquely characterizes the shock layer radiation independent of observer location. Currently, comparison of computational flowfield radiation results with the experimental observation data requires an additional post-processing step of converting the radiance solution to irradiance at observer's location including atmospheric effects [19, 24]. This work aims to eliminate the effect of observer's location by using the reconstructed trajectory information from observation and converting the spectral irradiance data to spectral radiance and emission coefficients, thereby direct comparison would be possible for a given view angle. Previous work by McIntyre et al. [5] has also presented Hayabusa reentry data in calibrated spectral radiance units from a ground observation including intervening atmospheric effects.

Attenuation of radiation due to atmospheric effects such as molecular absorption and Rayleigh scattering has also been accounted for in the present work. The view area of the capsule, which is dictated by the view angle, is computed to determine the continuum emission from the hot capsule surface. The spectral features due to atomic emission lines are from the gas species present in the shock layer. A representative shock layer volume was calculated, based on computational shock layer temperature contours, to estimate the emission coefficient of the atomic emission lines. Finally, uncertainty in the measured emission coefficients are calculated based on individual uncertainties in the constituting parameters such as irradiance data, shock layer volume, capsule distance, and atmospheric transmission.

## **II. Trajectory and Spectral Irradiance of Hayabusa2 SRC**

The reentering SRC was observed by various instruments onboard a Falcon 900 business jet, looking through the side windows of the aircraft. Hyper-Mono- and Hyper-IR-series instruments were designed with monochrome and color cameras respectively coupled with transmission spectrographs (300 lines/mm). A GBRG Bayer pattern color filter array is present in front of the sensors of the color cameras. Hence, each pixel in the color cameras acquired the spectral data in one of the three color channels – red, green, or blue. Since each color channel has its own characteristic sensitivity, data from each channel has to be processed individually and these channels can be treated as three different instruments. The spectrometers used to acquire the spectra data have sensitivity in the range 600 nm – 1200 nm, and the

nominal center wavelength varied from 760 nm – 885 nm as a result of deviation of the target from the optical axis due to manual tracking. The layout details of instruments and operators at each instrument station, and their performance parameters can be found in [16]. A schematic illustrating the observation scene and the viewing geometry parameters is shown in Fig. 1.

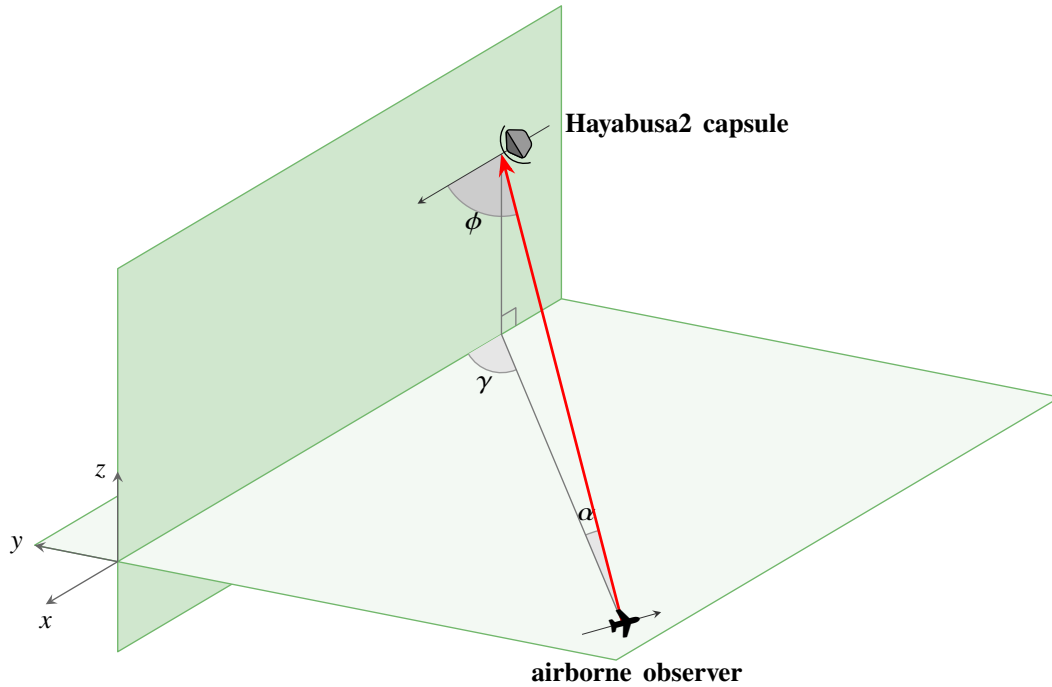


**Fig. 1** Definitions of line-of-sight (red arrow), azimuth ( $\gamma$ ), elevation ( $\alpha$ ), and view angle ( $\phi$ ). Object sizes and vectors are not to scale.

Instantaneous locations of the capsule and airborne observer are shown with their respective velocity vectors. Capsule’s velocity vector lies in  $xz$ -plane, the observer lies in  $xy$ -plane, and the  $z$ -axis is normal to the local sea level. The red arrow indicates the line-of-sight from the observer to the target capsule. The angle between the capsule’s velocity vector and the line-of-sight vector is termed as view angle ( $\phi$ ). The view angle can also be deduced from azimuth ( $\gamma$ ) and elevation ( $\alpha$ ) angles using the relation:  $\cos \phi = \cos \gamma \times \cos \alpha$ . The magnitude of the line-of-sight vector gives the instantaneous distance between the observer and the target object, termed as capsule distance ( $d_{obj}$ ). The SRC trajectory used in this work is taken from the analysis performed by Zander et al. [12] using the same airborne observation data. The locations of the capsule and the observer, and the lines-of-sight at 2 s time intervals during the visible part of the trajectory are plotted in geodetic coordinates in Fig. 2. From the trajectory, azimuth and elevation angles prescribe the projected view areas of the capsule and the shock layer. The projected area and the capsule distance are required to convert the radiation data from spectral irradiance to spectral radiance. These values are listed in Table 1, and plotted in Fig. 3. Details of capsule visible area calculations are explained in Section III.

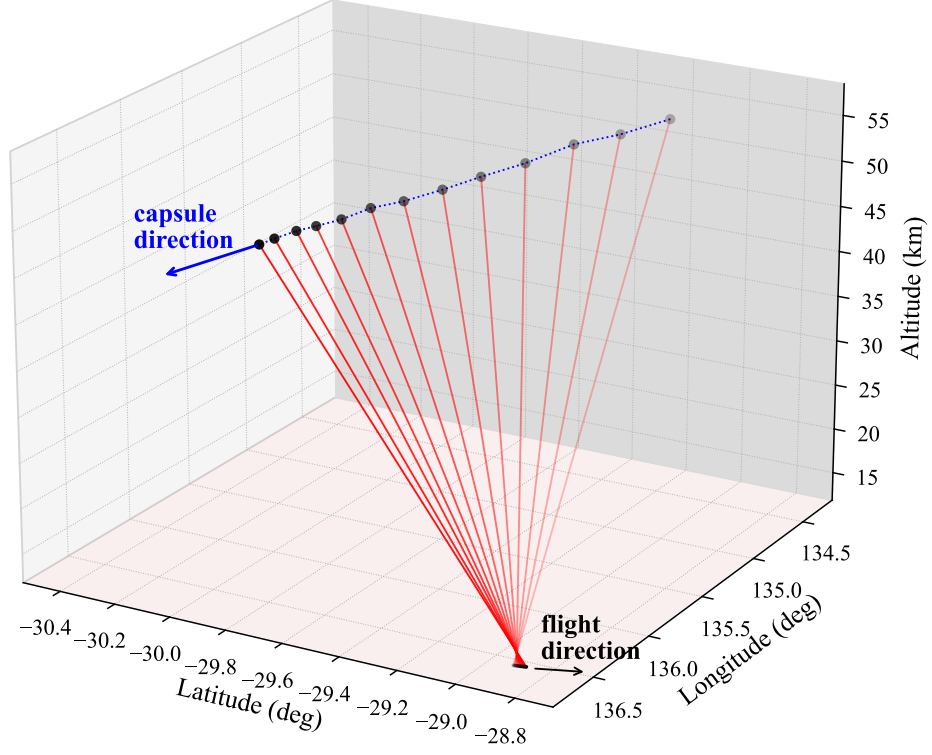


**Fig. 2** Latitude, longitude and altitude (lat, lon, alt) plot of the positions of Hayabusa2 SRC and Falcon 900 aircraft along the trajectory (17:29:02 – 17:29:26 UTC). Red lines indicate the line-of-sight vectors.

**Table 1** Parameters at each trajectory point

Trajectory #	Time UTC	Azimuth $\gamma$ ( $^{\circ}$ )	Elevation $\alpha$ ( $^{\circ}$ )	View angle $\phi$ ( $^{\circ}$ )	Capsule distance $d_{\text{obj}}$ (km)	Capsule view area $A_{\text{obj}}$ ( $\text{m}^2$ )
Point 0	17:29:02	65.69	11.00	66.16	197.68	$6.11 \times 10^{-2}$
Point 1	17:29:04	70.87	11.40	71.26	191.04	$5.58 \times 10^{-2}$
Point 2	17:29:06	76.41	12.16	76.72	186.38	$4.83 \times 10^{-2}$
Point 3	17:29:08	81.53	11.65	81.70	182.97	$4.11 \times 10^{-2}$
Point 4	17:29:10	87.19	11.95	87.25	181.51	$3.42 \times 10^{-2}$
Point 5	17:29:12	91.85	11.94	91.81	181.48	$2.98 \times 10^{-2}$
Point 6	17:29:14	96.74	11.87	96.60	182.67	$2.57 \times 10^{-2}$
Point 7	17:29:16	101.04	11.58	100.81	184.71	$1.98 \times 10^{-2}$
Point 8	17:29:18	103.93	12.02	103.62	187.14	$1.80 \times 10^{-2}$
Point 9	17:29:20	107.28	11.39	106.93	189.84	$1.46 \times 10^{-2}$
Point 10	17:29:22	109.61	11.18	109.22	192.34	$1.30 \times 10^{-2}$
Point 11	17:29:24	111.71	11.62	111.25	195.38	$1.14 \times 10^{-2}$
Point 12	17:29:26	113.27	11.76	112.75	197.74	$0.99 \times 10^{-2}$

The data acquired by various spectrometers from the airborne observation were then post-processed and calibrated in spectral irradiance units ( $\text{W m}^{-2} \text{nm}^{-1}$ ) by Birch et al. [13]. A 5 W calibration lamp in an integrating sphere

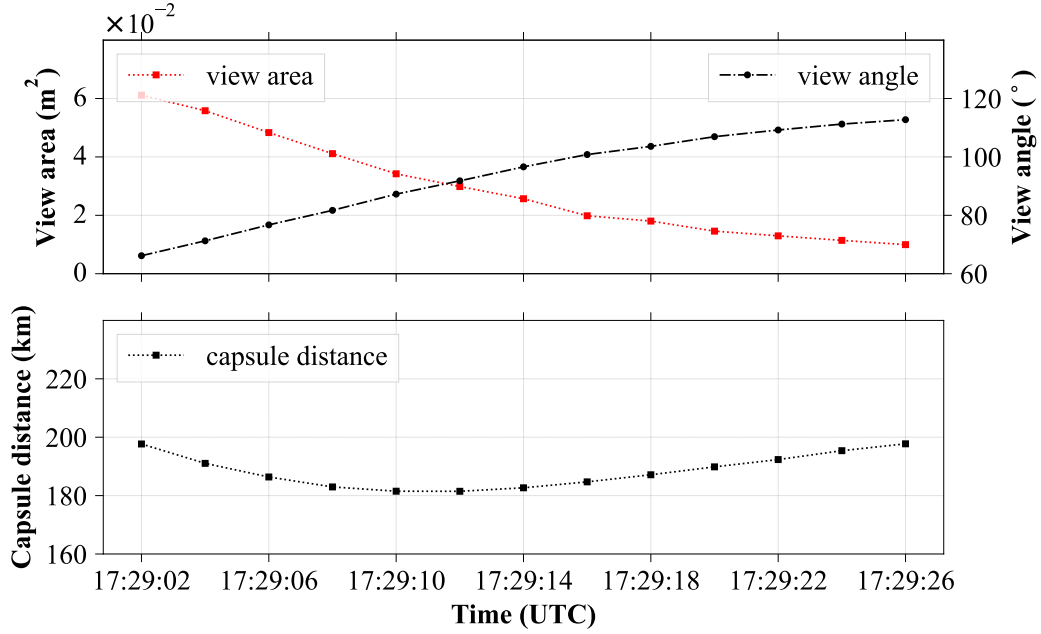


**Fig. 3** Time history of capsule surface view areas, view angles, and capsule distances for trajectory points #0 – #12.

(5.419 mm<sup>2</sup> circular aperture) was used as the calibration source. Wavelengths were identified from known emission lines using an AVANTES HgAr line source. Post-processing steps of the recorded spectral data include de-bayering red, green, and blue channels (for color cameras), image rotation and re-gridding, background subtraction, region-of-interest identification, intensity calibration, and pixel and wavelength alignment. Further details of the calibration steps can be found in [13]. The spectral data thus calibrated to spectral irradiance ( $\text{W m}^{-2} \text{nm}^{-1}$ ) have been inherited in this work, and further converted to spectral radiance ( $\text{W m}^{-2} \text{sr}^{-1} \text{nm}^{-1}$ ) and emission coefficient ( $\text{W m}^{-3} \text{sr}^{-1} \text{nm}^{-1}$ ) using the solid angle calculated from trajectory data. Data acquired by the instrument Hyper-IR-1 is taken for analysis in the rest of the paper.

### III. Spectral Radiance and Emission Coefficient Conversion of Hayabusa2 SRC

Spectral irradiance is a measure of the radiation as received by a detector located at a distance from the source whereas spectral radiance and emission coefficient of a source defines its absolute emission independent of its distance from the observer. Spectral radiance pertains to surface radiation (continuum emission from hot capsule surface) and emission coefficient is used to characterize the radiation emitted per unit volume of the source (radiation from atomic/molecular species in the shock layer). It should be noted that these quantities are defined for a given line-of-sight and as such the data discussed in this work pertains to the averaged value over the capsule surface/shock layer volume, owing to the point-source nature of the capsule given its distance.

The spectral radiance of the target object ( $L_{\lambda,\text{obj}}$ ) can be expressed in terms of spectral irradiance ( $E_{\lambda,\text{obj}}$ ) as

$$L_{\lambda,\text{obj}} = E_{\lambda,\text{obj}} \times \frac{d_{\text{obj}}^2}{A_{\text{obj}}} \quad (1)$$

The capsule distance ( $d_{\text{obj}}$ ) and the capsule's view area ( $A_{\text{obj}}$ ) are the two critical parameters which are required to convert the observation data in spectral radiance units. It can be noted that the spectral radiance of the object is independent of the detector area. The data inherited in this work is calibrated spectral irradiance, which is  $E_{\lambda,\text{obj}}$  in the above equation. It should also be noted that the calibrated spectral irradiance is the radiation that reaches the observer after being attenuated by the atmosphere present between the target and the observer. Radiation attenuated by atmospheric absorption can be corrected by using a calculated atmospheric transmission ( $\mathcal{T}_\lambda$ ) for a given observation geometry using Eq. 2.

$$L_{\lambda,\text{obj}} = E_{\lambda,\text{obj}} \times \frac{d_{\text{obj}}^2}{A_{\text{obj}}} \times \frac{1}{\mathcal{T}_\lambda} \quad (2)$$

The above relation can be used to obtain the spectral radiance of the atomic emission features when the emitting source is infinitely thin or when studying only the surface radiation. However, emission lines from atomic/molecular species originate from a volume of the shock layer which has a finite thickness. Hence, the above relation can be modified based on the volume of the emitting source (a portion of the shock layer in this case). To simplify the problem, the shock layer is assumed to be optically thin. The resulting parameter is spectral emission coefficient ( $j_{\lambda,\text{SL}}$ ) of the shock layer as given in Eq. 3.

$$j_{\lambda,\text{SL}} = L_{\lambda,\text{SL}} \times \frac{A_{\text{obj}}}{V_{\text{SL}}} \quad (3)$$

The term ( $L_{\lambda,\text{SL}}$ ) denotes the spectral radiance data after being decoupled from hot surface by subtracting the underlying Planck radiation. The volume of the shock layer can be represented as the projected surface area of the shock layer ( $A_{\text{SL}}$ ) multiplied by an equivalent depth of the shock layer ( $\delta_{\text{SL}}$ ) in the view direction, as given in Eq. 4.

$$j_{\lambda,\text{SL}} = L_{\lambda,\text{SL}} \times \frac{A_{\text{obj}}}{A_{\text{SL}}} \times \frac{1}{\delta_{\text{SL}}} \quad (4)$$

The resulting spectral emission coefficient is in the units of  $\text{W m}^{-3} \text{sr}^{-1} \text{nm}^{-1}$ . The Planck radiation subtraction and shock layer volume calculation are explained in Section IV.B.

### A. View Area of the SRC

One of the critical parameters in estimating the spectral radiance of the reentry body is the area of the capsule projected normal to the observer, termed as view area of the target object ( $A_{\text{obj}}$ ). The viewing geometry varies along the trajectory as the both the capsule and the airborne observer are dynamic. The resulting view area is prescribed by

the instantaneous azimuth and elevation angles. The surface geometry of the Hayabusa2 SRC was computationally divided into multiple triangular tile elements. For a combination of azimuth and elevation angles, the view area is calculated from the projection of those individual tile areas, as shown in Fig. 4. The projected area of each tile element is obtained by multiplying the tile surface area with the cosine of the angle between surface normal and line-of-sight. The total view area is then a summation of all tile elements in the region of interest. For our surface temperature analysis, the view areas for the visible TPS portion alone are calculated and given in Table 1. For the spectral features due to atomic emission lines, the view area of the shock layer accounting for high temperature shock layer region was used as explained in Section IV.B.

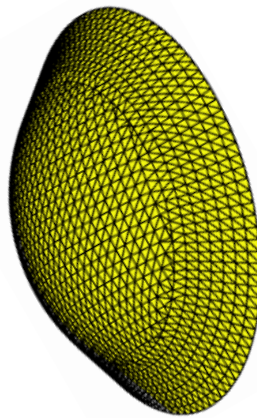


**Fig. 4 Model of the capsule's TPS surface at a view angle. Projection of individual tile elements are used to calculate total projected surface area.**

## **B. Atmospheric Attenuation of Emitted Radiation**

The emitted radiation from the target gets attenuated to a certain extent before reaching the observer as it traverses through the atmosphere. The amount of radiation that reaches the observer after atmospheric attenuation is governed by the wavelength dependent transmission of the atmospheric layer(s). Atmospheric correction models such as MODTRAN<sup>®</sup> [26], HITRAN [27], GEISA [28], and SpectralCalc [29], to name a few, are available to compute the atmospheric transmission for a given optical path in a given model of the atmosphere to varying degrees of fidelity. Radiation attenuation occurs mainly due to the atmospheric processes such as absorption by molecular species and Rayleigh scattering. Scattering due to aerosols is not considered here. In this work, PYTHON for Computational Atmospheric Spectroscopy (Py4CATS) [30], an open-source tool based on Python3 programming language, was used to compute the atmospheric absorption due to various molecular species (e.g., H<sub>2</sub>O, O<sub>2</sub>, N<sub>2</sub>, CO, CO<sub>2</sub>, N<sub>2</sub>O, and CH<sub>4</sub>). Attenuation due to Rayleigh scattering and ozone (O<sub>3</sub>) were calculated separately, and finally combined to obtain the

total transmission.

Py4CATS imports the line strengths of the chosen molecular species from either HITRAN or GEISA line strength database for the chosen wavelength (or wavenumber) range; here, the HITRAN database was used. Atmospheric properties, pressure, temperature, species concentration, and air number density are readily available in Py4CATS for various discrete altitudes ranging from bottom to top of the atmosphere. In other words, these properties are defined at  $m$  discrete altitude points starting from the bottom (0 km) to top of the atmosphere (100 km), where the atmosphere is divided into  $m - 1$  layers bounded by those points. For a 50-grid model (49-layered), the properties are available up to 120 km. In all of the models, the grid resolution is finer at lower parts of the atmosphere and it gets coarser as altitude increases. Various atmospheric models including mid-latitude summer, mid-latitude winter, tropical, US Standard, sub-arctic summer, and sub-arctic winter can also be specified along with the altitude resolution of the atmosphere. In our calculations, the 20-grid mid-latitude summer atmosphere was used.

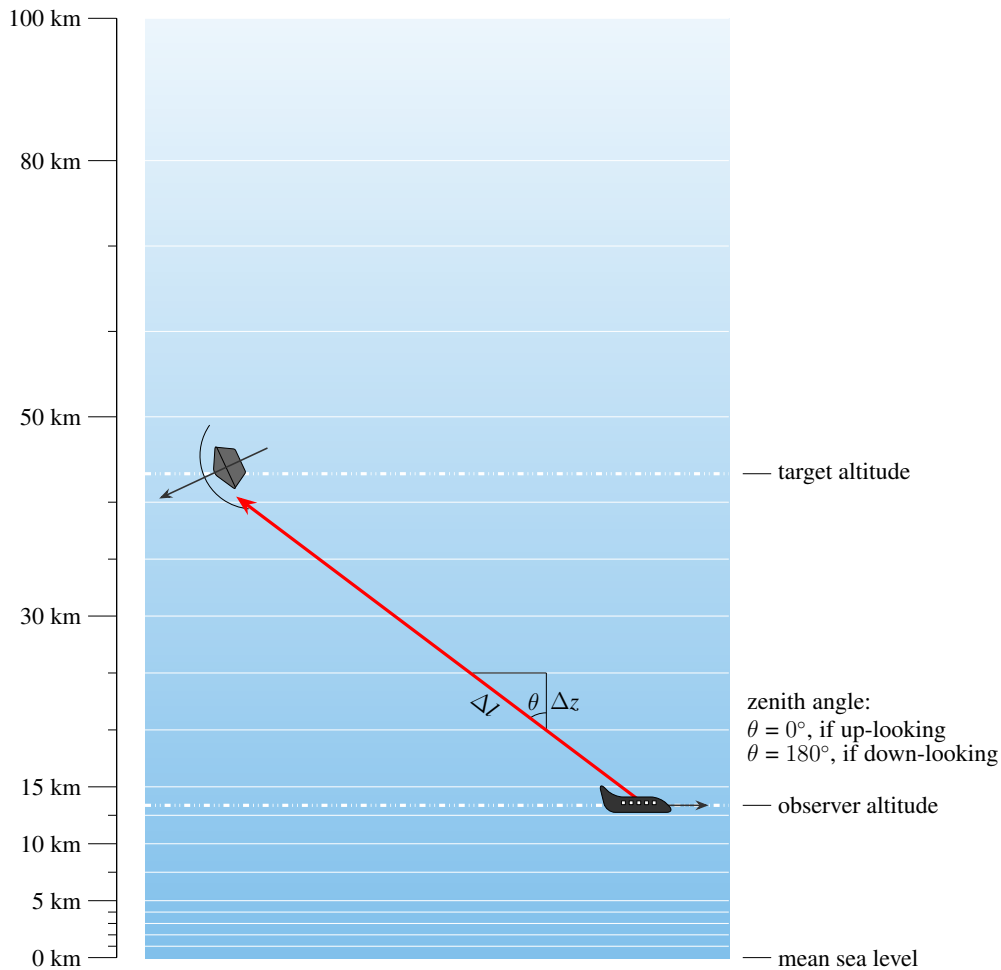


**Fig. 5 Schematic of the airborne observation scenario in a plane-parallel atmospheric model. Object sizes and vectors are illustration only, not to scale.**

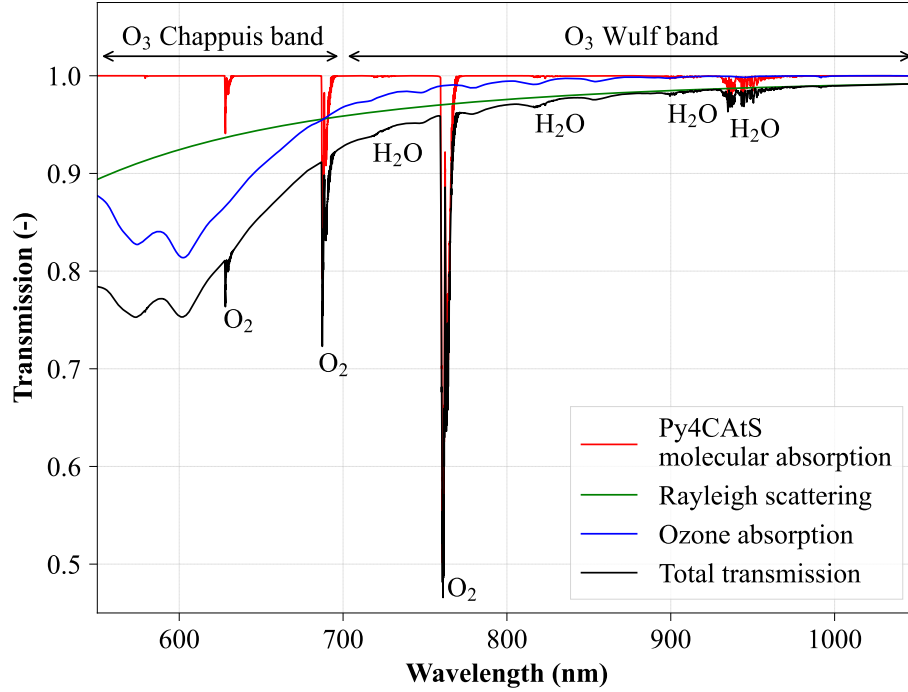
The airborne observation scenario superimposed on a 20-grid atmospheric model is schematically illustrated in

Fig. 5. The velocity vectors of the target and the observer are also marked by black arrows passing through them respectively. The red arrow illustrates the line-of-sight vector from the observer to the target. As both the observer and target are dynamic during the observation, the capsule distance ( $d_{\text{obj}}$ ) varies from 181 km – 198 km, see Table 1. Here, the atmosphere is modeled as a plane-parallel one where the curvature of the Earth is neglected and the atmosphere is assumed to be one-dimensional, bounded by horizontal plane surfaces at the top and bottom. The plane-parallel assumption is widely used in radiation models to simplify the calculation of radiation attenuation. As the observer and target altitudes may fall between pre-defined grid points, the atmospheric properties at those intermediate altitudes are interpolated and the atmosphere is then re-gridded by including those altitudes on a case-by-case basis. The original grid points are illustrated by solid white lines and the re-gridded points are shown as broken white lines; the altitude bounds of each atmospheric layer are also annotated.

In a plane-parallel atmosphere, for vertically up-looking or down-looking geometries, the optical path is simply the difference between the observer and target altitudes. As illustrated in Fig. 5, a zenith angle ( $\theta$ ) must be defined for airborne observation geometries, to account for the inclination of the line-of-sight so that the length of the optical path can be accurately estimated. The capsule distance segment ( $\Delta l$ ) in a given atmospheric layer is given by the relation:  $\Delta l = \Delta z / \cos \theta$ , where  $\Delta z$  is the thickness of a given atmospheric layer. Optical depth is a quantity that characterizes the strength of absorption in a medium and it is directly proportional to the length of the optical path. Optical depths from each atmospheric layer are then summed to obtain the integrated optical depth. Hence, for observation geometries with zenith angle ( $\theta$ ), the integrated optical depth along the line-of-sight is given by  $\tau_\lambda = \tau_{\lambda, \text{vertical}} / \cos \theta$ . The convention of zenith angle is  $0^\circ$  and  $180^\circ$  for up-looking and down-looking geometries respectively. The wavelength dependent transmission is then calculated from the integrated optical depth along the line-of-sight using the relation:  $\mathcal{T}_\lambda = e^{-\tau_\lambda}$ . The transmission of radiation after molecular absorption alone at trajectory point #0 (17:29:02 UTC) is shown in Fig. 6, as determined using Py4CATS. Absorption bands due to water (at 720 nm, 820 nm, 900 nm, and 937 nm) and oxygen molecules (at 628 nm, 687 nm, and 760 nm) are distinctly clear, as annotated in Fig. 6. The calculated transmission is shown for the wavelength range relevant to this work.

The absorption cross-sections ( $\sigma$  in  $\text{cm}^2$ ) for ozone in the wavelength range considered here was obtained from Ref. [31]. The cross-section data can be directly downloaded as ASCII file from the webpage [32] of Universität Bremen’s Molecular Spectroscopy and Chemical Kinetics Group. The cross-section data was available for a range of temperatures and the data was interpolated for temperatures in each atmospheric layer during transmission calculation. The optical depth was then integrated along the line-of-sight as before and the transmission due to ozone was obtained, as shown in Fig. 6. The two dominant absorption bands of ozone namely the Chappuis-band and Wulf-band are also annotated.

The cross-section for Rayleigh scattering can be defined as a function of wavelength following an empirical relation



**Fig. 6 Total transmission calculated for trajectory point #0 (17:29:02 UTC). Components due to molecular absorption (calculated by Py4CAAtS), ozone absorption, and Rayleigh scattering are also shown.**

by Bodhaine et al. (see Eq. (29) in Ref. [33]) as given below.

$$\sigma(\lambda) = \frac{1.045\,599\,6 - 341.290\,61\lambda^{-2} - 0.902\,308\,50\lambda^2}{1 + 0.002\,705\,988\,9\lambda^{-2} - 85.968\,563\lambda^2} \times 10^{-28} \text{ cm}^2 \quad (5)$$

From the scattering cross-section, the optical depth in a given atmospheric layer ( $\Delta\tau_\lambda$ ) can then be calculated using the relation:

$$\Delta\tau_\lambda = \sigma(\lambda) \times n \times \frac{\Delta z}{\cos \theta} \quad (6)$$

where,  $n$  is the air number density ( $\text{cm}^{-3}$ ) in a given atmospheric layer. The integrated optical depth was then obtained by the summation of optical depths in each layer. The resulting transmission due to Rayleigh scattering is also shown in Fig. 6. Finally, the total transmission was obtained as the product of these three transmission components. Similarly, the total transmission was calculated for trajectory points #0 – #12 and plotted in Fig. 7.

It can be noted that the transmission decreases along the trajectory as the target altitude decreases. Although the change in capsule distance was not significant along the trajectory, the change in atmospheric density and species concentration at those altitudes affects the resulting transmission. At lower target altitudes, the portion of line-of-sight lying in the denser atmospheric layer is larger compared to higher target altitudes.

As a verification of the atmospheric tool used in this work, the calculated transmission for a test case was compared

with that of MODTRAN<sup>®</sup>. The transmission for a trajectory point in Hayabusa1 mission was calculated using our tool, for an extended wavelength range (300 nm – 1700 nm), and was compared with the values calculated using MODTRAN<sup>®</sup> by Winter et al. [25], as shown in Fig. 8. The overall agreement was quite good with minor offset in the lower wavelength region possibly arising from the differences in ozone transmission calculations and/or due to the inclusion of aerosols in MODTRAN<sup>®</sup>. However, the maximum difference between the transmission values is within 5%, and the wavelength of interest in this work is > 600 nm.

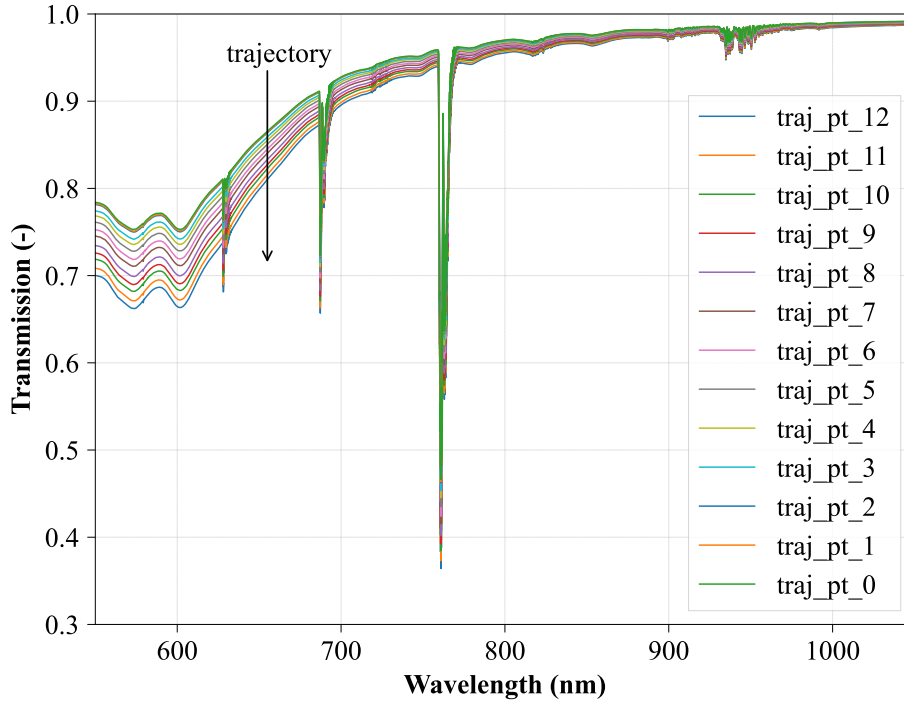


**Fig. 7 Total transmission values for trajectory points #0 – #12 (17:29:02 – 17:29:26 UTC).**

#### IV. Results and Discussion

The spectral irradiance data is converted to spectral radiance using the calculated solid angle and atmospheric transmission. Figure 9 shows the spectral data corresponding to trajectory point #0 at time 17:29:02 UTC from the red channel of Hyper-IR-1 spectrometer; calculated atmospheric transmission is shown at the top, spectral irradiance without atmospheric correction in the middle, and the converted spectral radiance with atmospheric correction at the bottom of the figure. Atomic emission lines of  $H_{\alpha}$  at 656.3 nm, N at 744 nm, 818 nm, and 868 nm, and O at 777 nm, 822 nm, and 845 nm are annotated. It is to be noted that annotations are to identify the spectral features and the calculated emission coefficients of those atomic features based on shock layer volume will be discussed in next subsection. The above spectral radiance conversion based on projected surface area of the capsule pertains only to the radiation emitted from the hot surface.

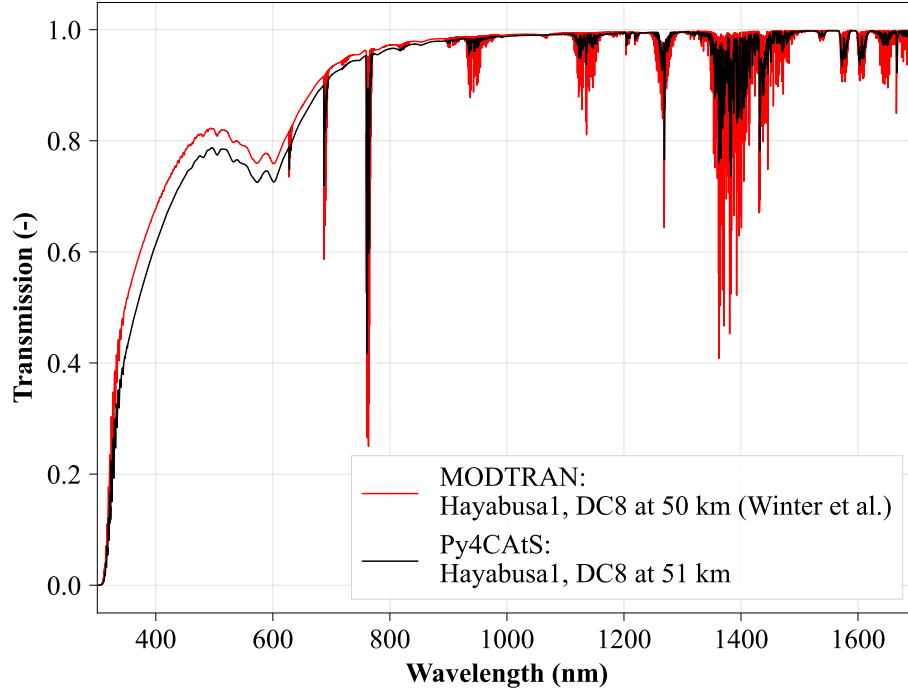


**Fig. 8** Verification of transmission values for Hayabusa1 test case with MODTRAN® data from Winter et al. [25].

### A. Surface Temperature Estimation

The converted (and atmospheric transmission corrected) spectral radiance is then used to determine the surface temperature of the capsule by least-squares curve fitting to the Planck function. Planck's law defines the radiation emitted by an object, with a surface emissivity ( $\epsilon$ ) and at temperature  $T$  (in K), as given in Eq. (7).

$$L(\lambda, T) = \epsilon \frac{2hc^2}{\lambda^5} \frac{1}{e^{hc/\lambda kT} - 1} \quad (7)$$

The spectral data recorded by the observer contains radiation from the shock layer due to molecular/atomic emission superimposed on the continuum Planck emission from the hot capsule surface. Due to the distant location of the capsule, it appears only as a point-source to the observer and spatially resolved spectral data cannot be directly measured. Hence, the spectral data contains lumped Planck emission arising from the view area that has spatially varying temperature distribution, and the spectral fit to Planck function can yield only a representative surface temperature. The representative temperature thus obtained is termed as apparent temperature ( $T_{app}$ ) [4].

Due to manual tracking of the spectrometers, the target object was not captured in all frames [13]. Useful data were obtained for the trajectory points #0 – #9 from Hyper-IR-1 spectrometer. The data from red channel of Hyper-IR-1 is used for Planck fitting as shown in Fig. 10. It can be noted that the spectral data contains peaks due to atomic lines that would affect the quality of the Planck fit. The spectral bandwidths corresponding to atomic emission lines were

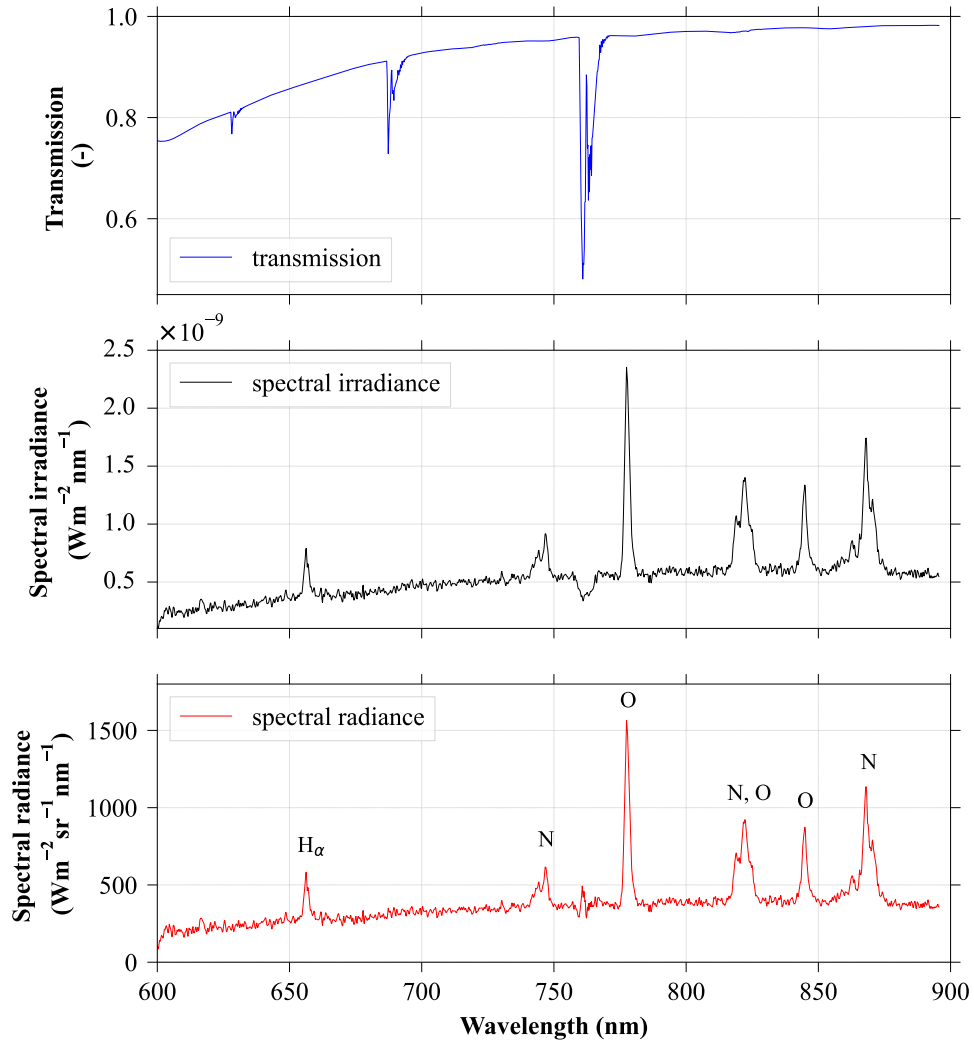


**Fig. 9 Spectral radiance with atmospheric absorption correction at trajectory point #0 (17:29:02 UTC). Spectral irradiance data is from the red channel of Hyper-IR-1 spectrometer.**

excluded from the data so that only continuum radiation data was used for Planck curve fitting. Figure 10 shows the transmission corrected spectral radiance, corresponding continuum data, and the resulting Planck curve fit for trajectory points #0 – #9. The time instance (UTC) and capsule altitudes of each data point are annotated.

The analysis was further extended by calculating the spatial distribution of surface temperature based on peak surface temperature identification method following Birch et al. [14]. This method employs a parameterized empirical model for surface temperature distribution. Synthetic spectra were generated using a Hayabusa capsule surface temperature distribution and fitted to the intensity generated by using an empirical temperature distribution with a predefined maximum temperature. This results in identifying a peak surface temperature ( $T_{\text{peak}}$ ) and a surface temperature distribution. More details on the empirical model and surface temperature distribution can be found in [14]. The estimated surface temperature distribution at trajectory point #2 is shown in Fig 11.

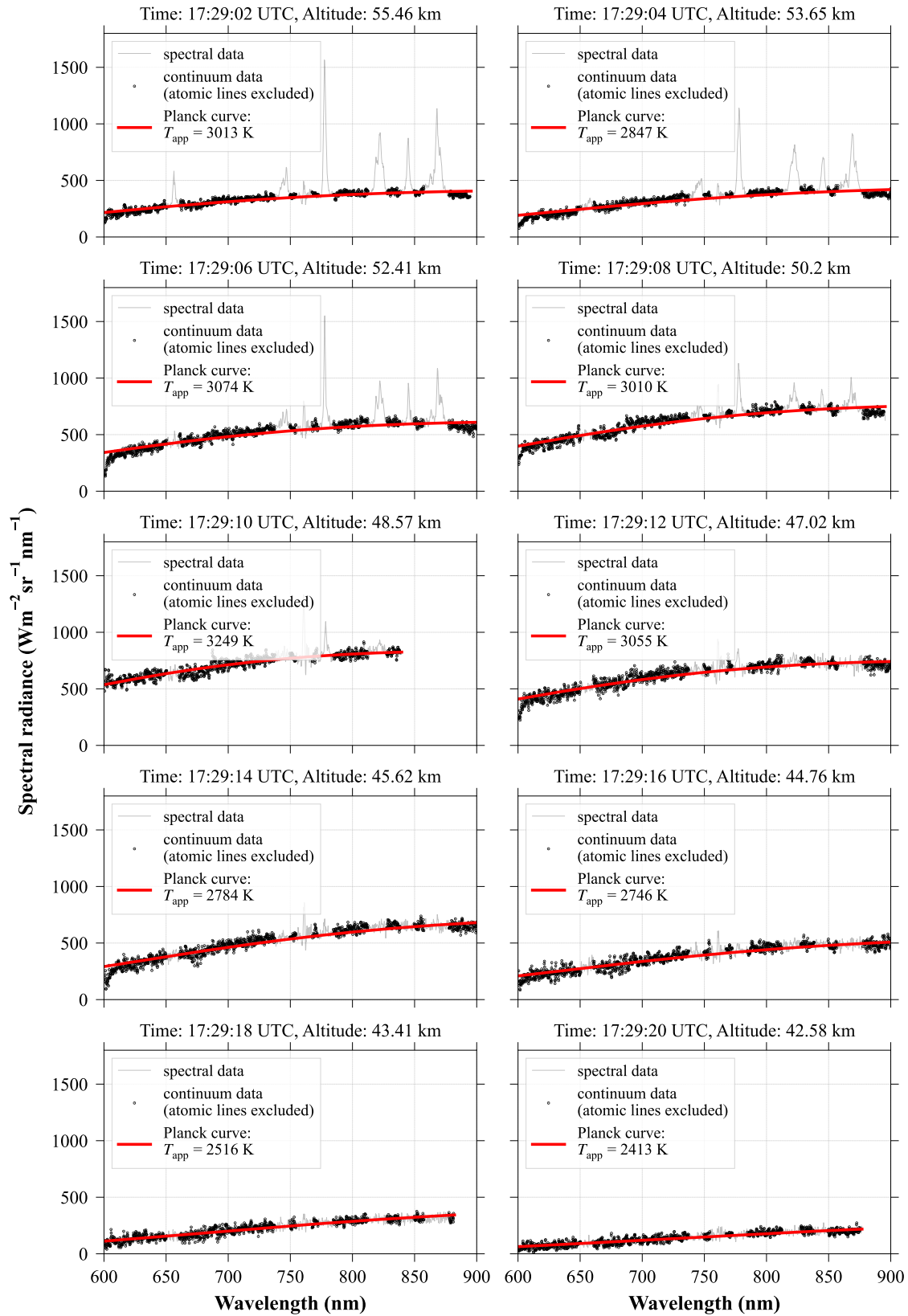


**Fig. 10** Spectral data of Hayabusa2 SRC (gray lines) at trajectory points #0 – #9 (UTC 17:29:02 – 17:29:20). Continuum data are shown as black dots and the resulting Planck curve fits as red lines.

The peak and apparent temperature estimates from Hyper-IR-1 red channel data for all useful frames are plotted in Fig. 12. It can be noted that there is an offset between peak and apparent temperatures throughout the trajectory. Along the trajectory, the view angle increases and the projected view area decreases (see Fig. 3). The effect of view angle, though minimal, can be noticed from the ratio of peak and apparent temperatures shown at the bottom of Fig. 12.

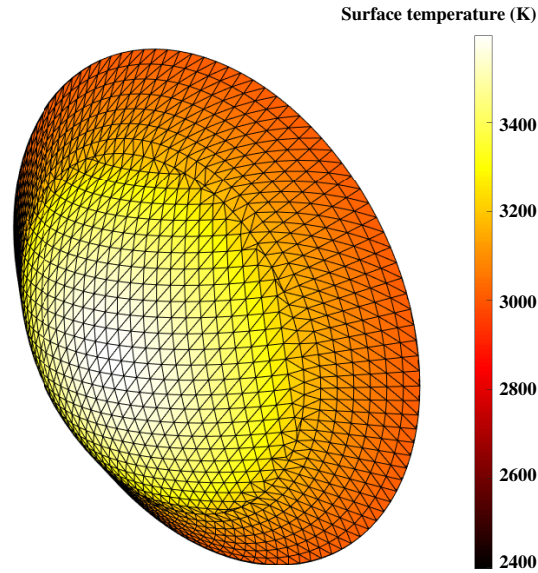


**Fig. 11 Spatial distribution of surface temperature at trajectory point #2 (17:29:06 UTC) estimated from peak temperature identification method [14].**

## **B. Spectral Emission Coefficient of Atomic Lines**

The spectral radiance data discussed thus far is based on the projected area of the capsule surface. This is generally applicable to study the continuum radiation from the hot capsule surface and is used to estimate the surface temperature distribution. The spectral peaks due to atomic emission lines originate from the gas species present in the engulfing shock layer, not from the capsule surface. Hence, when quantifying the spectral features from the atomic emission lines, the projected area of the capsule surface is not applicable. Here, a three-dimensional shock layer volume has to be considered to determine the magnitude of atomic line emission, see Eq. 4. However, this is not straightforward as the visible volume of the shock layer has to be calculated three-dimensionally at each view angle.

To simplify the problem, the atomic lines were assumed to be emitted from a portion of the shock layer where the temperatures are higher than 7000 K. At temperatures above 7000 K, it can be safely assumed that the oxygen and nitrogen molecules have already started to dissociate and their corresponding atomic species are available in the shock layer. A computational shock layer temperature contour in front of Hayabusa capsule at 53 km altitude from Winter et al. [25] was adapted in this work. A 2D profile bounding the shock layer region with temperatures above 7000 K was adapted in to Autodesk Fusion 360 and revolved by 360° to obtain a three-dimensional shock layer volume. Only a

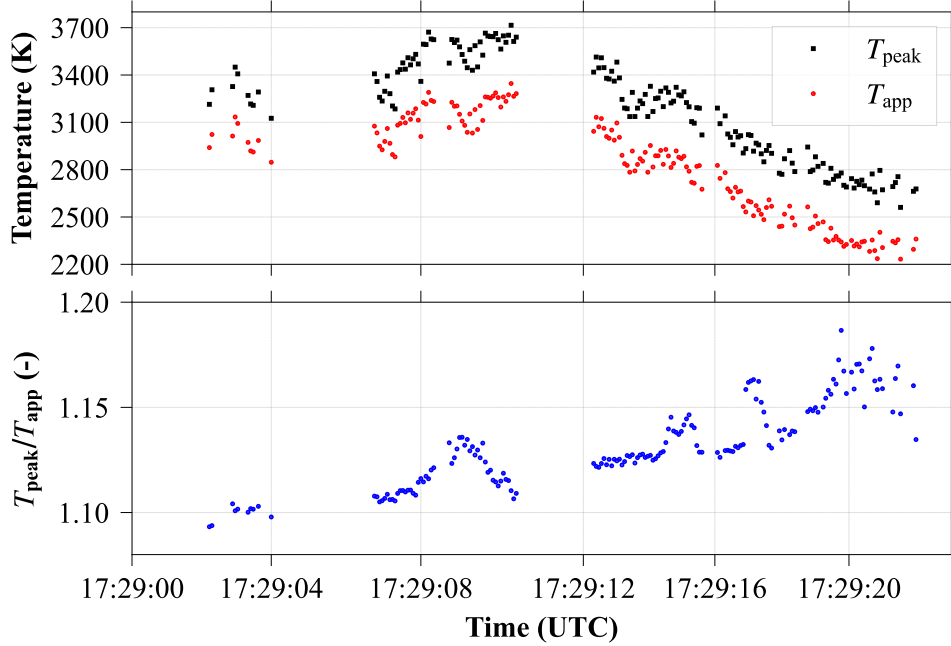


**Fig. 12 Apparent and peak surface temperatures estimated from all useful frames of Hyper-IR-1 spectrometer red channel.**

fraction of this volume is visible to an observer at a given view angle and the rest of it will be obscured by the underlying capsule surface. A graphical illustration of the visible shock layer volume at various view angles along the trajectory is shown in Fig. 13. Capsule geometry is only limited to front-half for illustration (shown in black). The fraction of visible volume at each view angle is calculated by multiplying the shock layer volume with the view factor of the shock layer projected area at the given view angle. The spectral radiance data of atomic lines from the shock layer ( $L_{\lambda,SL}$ ) was decoupled from hot surface radiation by subtracting the Planck curve from the spectral radiance received from the target object ( $L_{\lambda,obj}$ ). The spectral data recorded is the radiation emitted from the projected shock layer area ( $A_{SL}$ ) integrated over the equivalent depth of the shock layer ( $\delta_{SL}$ ) in the view direction.

The spectral radiance data of the shock layer was then used to calculate the spectral emission coefficients, following Eq. 4, for selected atomic species at various trajectory points and are shown comparatively in Fig. 14. The time evolution of intensity of atomic emission of various species can be seen. With increase in time, the emission intensity from atomic lines gradually reduces as the view angle increases. It is also partly due to the change in altitude and the velocity of the capsule, and hence the shock strength.

The calculated spectral emission coefficient can then be integrated over a wavelength region for dominant spectral features such as  $H_{\alpha}$  line at 656 nm, N line at 744 nm, O line at 777 nm, and N, O lines at 820 nm. The values were integrated over the wavelength bounding those lines and plotted for each atomic line from three color channels (red, green, and blue) in Fig. 15. The shaded regions around each color channel data indicate the calculated uncertainty



**Fig. 13** Projection at four different arbitrary view angles of a portion of shock layer volume where temperatures are above 7000 K (shown in beige).

bounds as explained in Section V.

It can be noted that the emission coefficient of atomic lines decrease along the trajectory. It approaches zero at view angles beyond  $100^\circ$  (after UTC 17:29:16) as majority of the shock layer from which these lines originate from is no longer in the view; moreover, the altitude and velocity also decrease along the trajectory. Generally, the qualitative agreement between all three color channels is good. For  $H_\alpha$  line, the emission coefficient from blue channel is not in agreement with the other two due to the noise in the spectral data. The differences could also be due to the measurement noise and the difference in sensitivity of each channel in the wavelength range 600 nm – 830 nm. Among the three color channels, blue channel has the lowest sensitivity and hence its estimates show bigger offsets from the estimates of other two channels. Beyond 830 nm and up to 1050 nm, all three color channels have almost identical sensitivity.

As shown in Fig. 14, the spectral peak of N at 744 nm is not as distinct as the other peaks (for example, O 777 and N 818) except for the first few trajectory points. This is reflected in the lower values of integrated radiance for N 744 nm line and offsets from each color channel, see Fig. 15. Data from all three channels were in good agreement for dominant spectral features such as O 777 nm and N, O 820 nm peaks.

## V. Uncertainty in Calculated Emission Coefficients

The uncertainty in the calculated emission coefficient is influenced by the individual uncertainties arising from the parameters, specifically irradiance data, capsule distance, shock layer volume, and atmospheric transmission, as evident from Eq. 4. The uncertainty in the irradiance data can be attributed mainly to the calibration source uncertainty, and to some extent, the variation in capsule's position in a given image array due to manual tracking. Based on the integrating sphere used for calibration, the uncertainty in irradiance data was taken to be -5% to +5%, neglecting the uncertainty due to variation in target position. The upper and lower bounds of the capsule distance and the capsule altitude were taken from the Hayabusa2 trajectory analysis by Zander et al. [12]. The capsule distance and altitude bounds were used to calculate the uncertainty in zenith angle, which in turn dictates the uncertainty in atmospheric transmission. It is to be noted that the transmission uncertainty varies with wavelength and only the highest value is taken. The uncertainty in

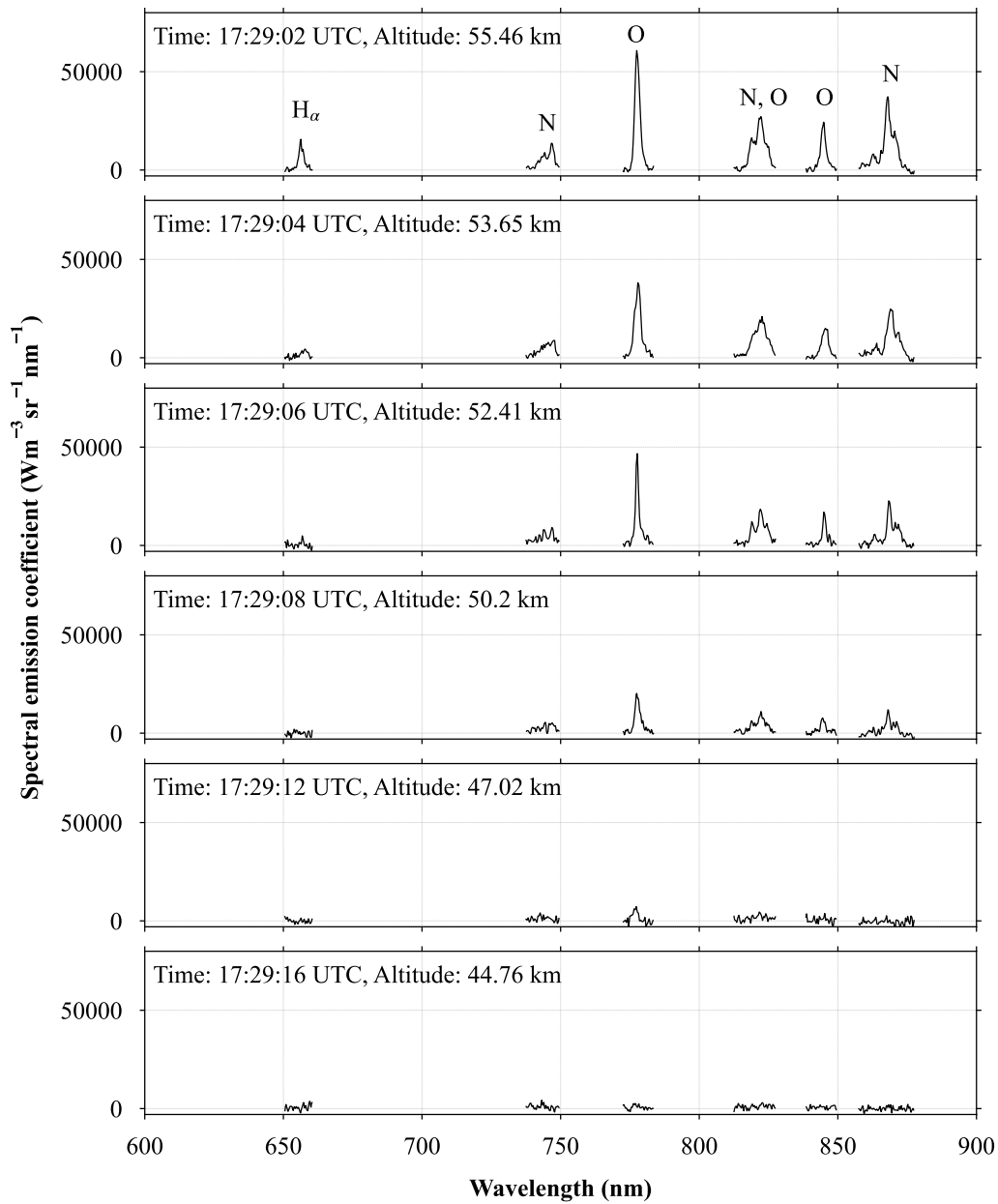


**Fig. 14** Spectral emission coefficients of selected atomic lines based on shock layer volume at various time instances.

emission coefficient due to transmission uncertainty is calculated to be -3% to -18% as the lower bound and +4% to +30% as the upper bound through the trajectory, as shown in Fig. 16. The shock layer visible volume is dictated by the view angle. The upper and lower bounds of view angles were estimated from the upper and lower bounds of capsule altitude. In all these calculations, the observer altitude was used without uncertainty. The uncertainty in view angles were used to calculate the uncertainty in shock layer visible volume. Finally, the total uncertainty in emission coefficient

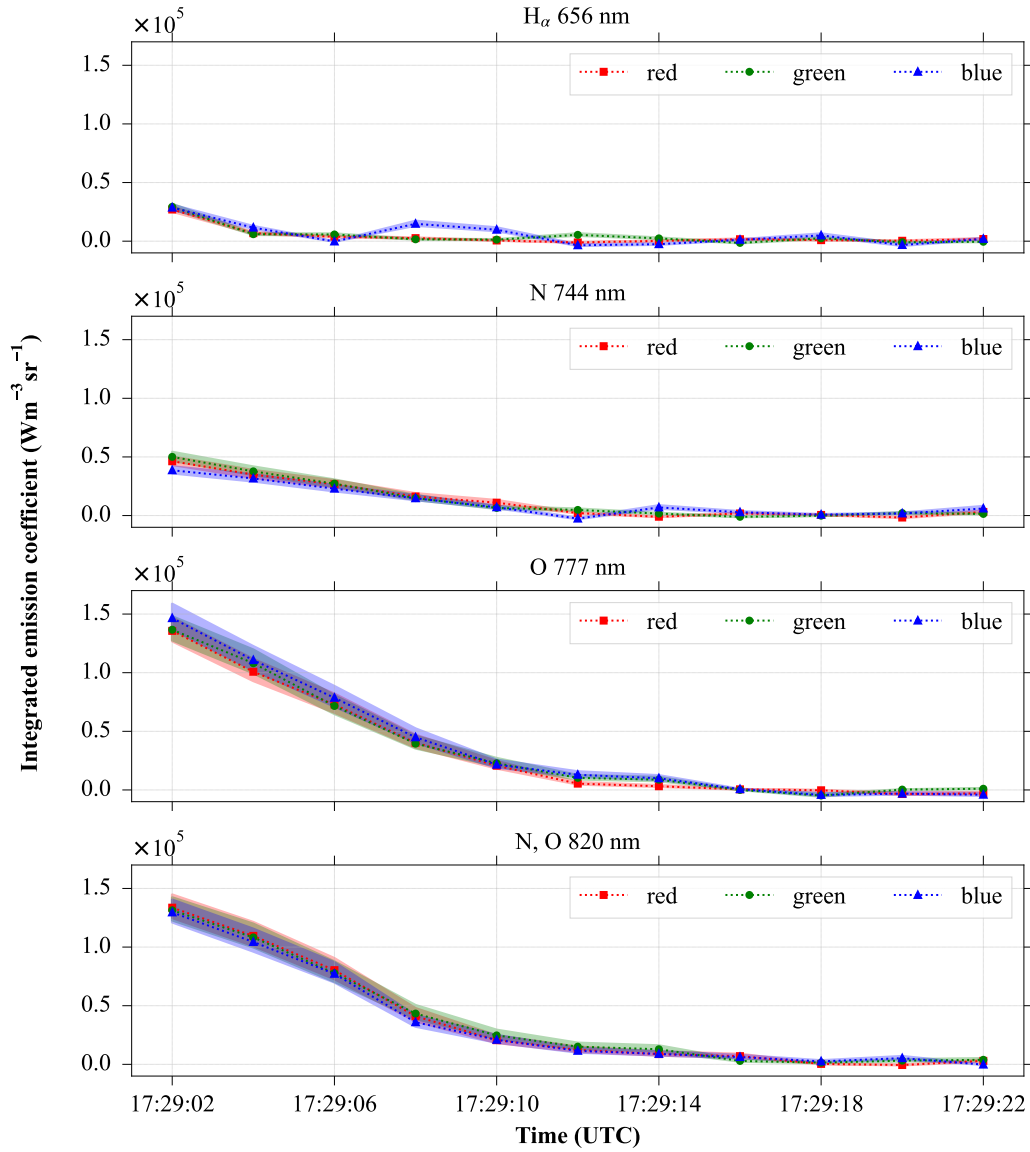


**Fig. 15** Emission coefficients of selected atomic lines at trajectory points #0 – #9 from red, green, and blue color channels of Hyper-IR-1 spectrometer.

is calculated as the root sum square of these individual uncertainties and plotted in Fig. 16, along with the distribution of individual uncertainties.

## VI. Conclusion

The Hayabusa2 reentry event was observed by the Australian Airborne Observation team with a range of spectral and video imaging instruments. The recorded data is converted into spectral radiance and emission coefficient terms using the previously reported trajectory data and spectral irradiance data. The effect of atmospheric absorption of emitted radiation is corrected by a calculated atmospheric transmission function using an open-source atmospheric

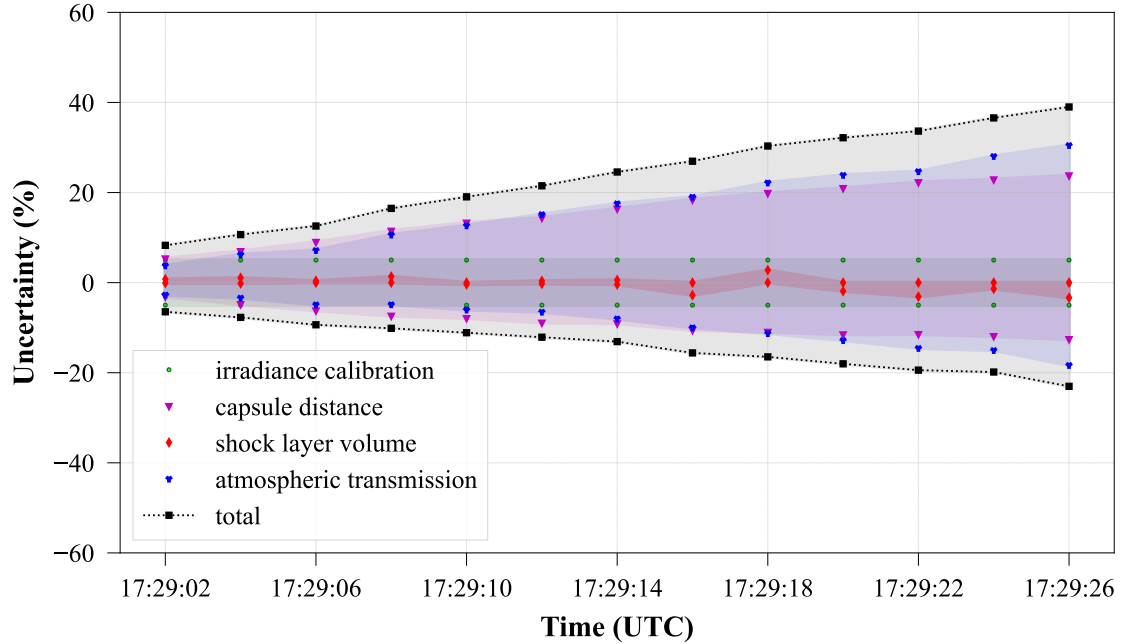


**Fig. 16 Total uncertainty distribution in emission coefficients of atomic species along the trajectory plotted with individual uncertainties.**

absorption calculator. The absorption corrected spectral radiance datasets were fit to a Planck function to estimate the apparent surface temperature at various time instances during the trajectory where useful data were recorded. The apparent temperature obtained from the least-squares fit is only representative, neglecting the spatial distribution of temperature across the view area of the capsule. The converted data was further used in combination with a parameterized empirical model to identify a peak surface temperature and a spatial distribution of surface temperature. A maximum peak temperature of 3700 K was observed at an altitude of approximately 48.6 km (17:29:10 UTC). Peak surface temperatures are approximately 300 K higher than apparent temperatures throughout the trajectory. Surface temperature measurements and estimates of Hayabusa SRC from other works were within the range of 2640 K – 3370 K. The maximum apparent surface temperature identified in this work is approximately 3350 K, and it is comparable to the higher end of the Hayabusa surface temperature values reported in the literature.

The conversion of spectral radiance was based on instantaneous projected view areas of the capsule surface, which is applicable to surface radiation from the hot capsule. To convert the radiation from atomic species present in the shock layer into emission coefficients, instantaneous shock layer view areas were used by considering a portion of the visible shock layer volume where temperature is expected to exceed 7000 K. The spectral data was subtracted by the calculated Planck curve to decouple the surface radiation from atomic emission lines. The Planck subtracted data was then used to calculate the emission coefficients of  $H_{\alpha}$  line at 656 nm, O line at 777 nm, and N lines at 744 nm and 820 nm. Emission coefficients of individual lines were integrated over their respective wavelength bands to obtain the time history of

intensity along the trajectory. A total uncertainty in emission coefficients of -23% to +39% was estimated based on individual uncertainties in the parameters such as capsule distance, irradiance data, visible shock layer volume, and atmospheric transmission.

The conversion of the surface and shock layer emission data to spectral radiance and spectral emission coefficients with atmospheric transmission correction presents the observation data independent of observer's location. This should enable direct comparison of numerical data for a given view angle without having to convert it to spectral irradiance at observer's location. However, it should be noted that the converted data presented here is still an integrated value for a given view angle and the spatial distribution of radiation is not deconvolved in the present approach. This will be addressed in future work. Accuracy in the surface and shock layer emission data lies not just on the accuracy in spectral calibration of the recorded data but also on the accuracy of the estimated trajectory parameters. The analysis presented here also demonstrates the value of taking up such observation campaigns and the resulting radiation and trajectory datasets.

## Acknowledgments

Fabian Zander was funded by the Australian Research Council's Discovery Early Career Researcher Award (DECRA) through award number DE200101674. The Australian Airborne Observation of Hayabusa2 was supported by Rocket Technologies International. Support from the University of Southern Queensland's electrical and mechanical workshops, Oliver Kinder, Stephanie Piper, Graham Holmes and Peter Schubel is gratefully acknowledged.

## References

- [1] Winter, M., and Herdrich, G., "Spectroscopic Observation of the STARDUST Re-Entry in the Near UV," *39th AIAA Thermophysics Conference*, AIAA Meeting Paper, 2007, p. 4050. <https://doi.org/10.2514/6.2007-4050>.
- [2] Jenniskens, P., Wercinski, P., Olejniczak, P., Wright, M., Raiche, G., Kontinos, D., Desai, P., Spalding, R., Sandquist, K., Rossano, G., Russel, R., Revelle, D., Hladiuk, D., and Hilderbrand, A., "Surface Heating from Remote Sensing of the Hypervelocity Entry of the NASA GENESIS Sample Return Capsule," *44th AIAA Aerospace Sciences Meeting and Exhibit*, AIAA Meeting Paper, 2006, p. 381. <https://doi.org/10.2514/6.2006-381>.
- [3] Löhle, S., Zander, F., Lemmens, S., and Krag, H., "Airborne Observations of Re-entry Break-up: Results and Prospects," *7th European Conference on Space Debris*, ESA, 2017. URL <https://api.semanticscholar.org/CorpusID:56261314>.
- [4] Buttsworth, D., Morgan, R., and Jenniskens, P., "Near-Ultraviolet Emission Spectroscopy of the Hayabusa Reentry," *Journal of Spacecraft and Rockets*, Vol. 50, No. 6, 2013, pp. 1109–1120. <https://doi.org/10.2514/1.A32500>.
- [5] McIntyre, T. J., Khan, R., Eichmann, T. N., Upcroft, B., and Buttsworth, D., "Visible and Near Infrared Spectroscopy of Hayabusa Reentry Using Semi-Autonomous Tracking," *Journal of Spacecraft and Rockets*, Vol. 51, No. 1, 2014, pp. 31–38. <https://doi.org/10.2514/1.A32497>.

- [6] Löhle, S., and Jenniskens, P., “High-Resolution Spectroscopy of the Hayabusa Reentry Using a Fabry–Perot Interferometer,” *Journal of Spacecraft and Rockets*, Vol. 51, No. 6, 2014. <https://doi.org/10.2514/1.A32480>.
- [7] Löhle, S., Mezger, A., and Fulge, H., “Measured Surface Temperatures of the Hayabusa Capsule during Re-entry Determined from Ground Observation,” *Acta Astronautica*, Vol. 84, 2013, pp. 134–140. <https://doi.org/10.1016/j.actaastro.2012.11.004>.
- [8] Löhle, S., Eberhart, M., Zander, F., Meindl, A., Rudawska, R., Koschny, D., Zender, J., Dantowitz, R., and Jenniskens, P., “Extension of the Plasma Radiation Database PARADE for the Analysis of Meteor Spectra,” *Meteoritics and Planetary Science*, Vol. 56, No. 2, 2021, pp. 352–361. <https://doi.org/10.1111/maps.13622>.
- [9] Jenniskens, P., Albers, J., Koop, M. W., Odeh, M. S., Al-Noimy, K., Al-Remeithi, K., Al Hasmi, K., Dantowitz, R. F., Gasdia, F., Löhle, S., Zander, F., Hermann, T., Farnocchia, D., Chesley, S. R., Chodas, P. W., Park, R. S., Giorgini, J. D., Gray, W. J., Robertson, D. K., and Lips, T., “Airborne Observations of an Asteroid Entry for High Fidelity Modeling: Space Debris Object WT1190F,” *AIAA Science and Technology Forum and Exposition (SciTech 2016)*, AIAA Meeting Paper, 2016. <https://doi.org/10.2514/6.2016-0999>.
- [10] Vaubaillon, J., Kotten, P., Margonis, A., Toth, J., Rudawska, R., Gritsevich, M., Zender, J., McAuliffe, J., Pautet, P., Jenniskens, P., Koschny, D., Colas, F., Bouley, S., Maquet, L., Leroy, A., Lecacheux, J., Borovicka, J., Watanabe, J., and Oberst, J., “The 2011 Draconids: The First European Airborne Meteor Observation Campaign,” *Earth, Moon, and Planets*, Vol. 114, 2015, pp. 137–157. <https://doi.org/10.1007/s11038-014-9455-5>.
- [11] Vaubaillon, J., Loir, C., Ciocan, C., Kandeepan, M., Millet, M., Cassagne, A., Lacassagne, L., Da Fonseca, P., Zander, F., Buttsworth, D., Loehle, S., Toth, J., Gray, S., Moingeon, A., and Rambaux, N., “A 2022  $\tau$ -Herculid Meteor Cluster from an Airborne Experiment: Automated Detection, Characterization, and Consequences for Meteoroids,” *Astronomy & Astrophysics*, Vol. 670, No. A86, 2023. <https://doi.org/10.1051/0004-6361/202244993>.
- [12] Zander, F., Buttsworth, D. R., Birch, B., and Payne, A., “Trajectory Analysis of the Hayabusa2 Capsule from a Single Airborne Observation,” *Journal of Spacecraft and Rockets*, Vol. 61, No. 1, 2023. <https://doi.org/10.2514/1.A35719>.
- [13] Birch, B., Zander, F., Buttsworth, D., Noller, L., and Payne, A., “Hayabusa2 Capsule Reentry: Visible and Near-IR Emission Spectroscopy from the Australian Airborne Observation,” *AIAA AVIATION Forum*, AIAA, Chicago, IL, 2022, p. 3736. <https://doi.org/10.2514/6.2022-3736>.
- [14] Birch, B., Buttsworth, D., and Zander, F., “Improved Surface Temperature Identification Method for Remote Observations of Sample Return Capsules,” *Journal of Spacecraft and Rockets*, Vol. 61, No. 2, 2024. <https://doi.org/10.2514/1.A35692>.
- [15] Yamada, T., “Best Estimated Trajectory and Attitude Motion of Hayabusa2 SRC Reentry Flight,” *AIAA AVIATION Forum*, AIAA, Chicago, IL, 2022, p. 3801. <https://doi.org/10.2514/6.2022-3801>.
- [16] Zander, F., Buttsworth, D. R., Birch, B., Noller, L., Wright, D., James, C. M., Thompson, M., Leis, J., Lobsey, C., and Payne, A., “Australian Rapid-Response Airborne Observation of the Hayabusa2 Reentry,” *Journal of Spacecraft and Rockets*, Vol. 58, No. 6, 2021, pp. 1915–1919. <https://doi.org/10.2514/1.A35062>.

- [17] Zander, F., Buttsworth, D., Birch, B., and Payne, A., "Planning and Implementation of the Australian Airborne Observation of Hayabusa2," *AIAA AVIATION Forum*, AIAA, Chicago, IL, 2022, p. 3583. <https://doi.org/10.2514/6.2022-3583>.
- [18] James, C. M., Liu, Y., Thompson, M., and Apirana, S., "University of Queensland Near Infrared Spectroscopy of the Hayabusa2 Re-entry," *AIAA AVIATION Forum*, AIAA, Chicago, IL, 2022, p. 3735. <https://doi.org/10.2514/6.2022-3735>.
- [19] Prabhu, D. K., Saunders, D., Cruden, B. A., and Grinstead, J., "Simulations of Hayabusa2 Atmospheric Entry and Comparisons with Data from the Imaging Campaign," *AIAA AVIATION Forum*, AIAA, Chicago, IL, 2022, p. 3800. <https://doi.org/10.2514/6.2022-3800>.
- [20] Scott, C. F., and Inman, J. A., "SCIFLI Airborne Observation of the Hayabusa2 Sample Return Capsule Re-Entry," *AIAA AVIATION Forum*, AIAA, Chicago, IL, 2022, p. 3798. <https://doi.org/10.2514/6.2022-3798>.
- [21] Scriven, G. R., Scott, C. F., Inman, J. A., Tanno, H., Yamada, T., Johnston, C. O., Prabhu, D. K., and Conn, R., "Hayabusa2 SHARC Spectro-Radiometric Calibration and Analysis," *AIAA AVIATION Forum*, AIAA, Chicago, IL, 2022, p. 3802. <https://doi.org/10.2514/6.2022-3802>.
- [22] Tanno, H., Yamada, T., Dantowitz, R., Klemm, C., Scott, C. F., Inman, J. A., Scriven, G. R., and Grinstead, J., "Analysis of Surface Temperature of Hayabusa1 & 2 SRC in Airborne Spectroscopy Measurement," *AIAA AVIATION Forum*, AIAA, Chicago, IL, 2022, p. 3733. <https://doi.org/10.2514/6.2022-3733>.
- [23] Tanno, H., Yamada, T., Dantowitz, R., Klemm, C., Scott, C. F., Inman, J. A., Scriven, G. R., and Grinstead, J., "Comparison of Flight and Shock Tunnel Spectroscopy of Hayabusa2 Sample Return Capsule," *AIAA AVIATION Forum*, AIAA, Chicago, IL, 2022, p. 3734. <https://doi.org/10.2514/6.2022-3734>.
- [24] Johnston, C. O., "Comparison between Hayabusa 2 Spectral Measurements and Simulations," *AIAA AVIATION Forum*, AIAA, Chicago, IL, 2022, p. 3799. <https://doi.org/10.2514/6.2022-3799>.
- [25] Winter, M. W., McDaniel, R. D., Chen, Y., Saunders, D., and Jenniskens, P., "Radiation Modeling for Reentry of Hayabusa Sample Return Capsule," *Journal of Spacecraft and Rockets*, Vol. 56, No. 4, 2019. <https://doi.org/10.2514/1.A34381>.
- [26] MODerate resolution atmospheric TRANsmission, 2014. URL [http://modtran.spectral.com/modtran\\_index](http://modtran.spectral.com/modtran_index), retrieved 01 May 2024.
- [27] Gordon, I. E., Rothman, L. S., Hargreaves, R. J., Hashemi, R., Karlovets, E. V., Skinner, F. M., Conway, E. K., Hill, C., Kochanov, R. V., Tan, Y., Wcislo, P., Finenko, A. A., Nelson, K., Bernath, P. F., Birk, M., Boudon, V., Campargue, A., Chance, K. V., Coustenis, A., Drouin, B. J., Flaud, J., Gamache, R. R., Hodges, J. T., Jacquemart, D., Mlawer, E. J., Nikitin, A. V., Perevalov, V. I., Rotger, M., Tennyson, J., Toon, G. C., Tran, H., Tyuterev, V. G., Adkins, E. M., Baker, A., Barbe, A., Canè, E., Császár, A. G., Dudaryonok, A., Egorov, O., Fleisher, A. J., Fleurbaey, H., Foltynowicz, A., Furtenbacher, T., Harrison, J. J., Hartmann, J., Horneman, V., Huang, X., Karman, T., Karns, J., Kass, S., Kleiner, I., Kofman, V., Kwabia-Tchana, F., Lavrentieva, N. N., Lee, T. J., Long, D. A., Lukashevskaya, A. A., Lyulin, O. M., Makhnev, V. Y., Matt, W., Massie, S. T.,

- Melosso, M., Mikhailenko, S. N., Mondelain, D., Müller, H. S. P., Naumenko, O. V., Perrin, A., Polyansky, O. L., Raddaoui, E., Raston, P. L., Reed, Z. D., Rey, M., Richard, C., Tóbiás, R., Sadiek, I., Schwenke, D. W., Starikova, E., Sung, K., Tamassia, F., Tashkun, S. A., Vander Auwera, J., Vasilenko, I. A., Vigasin, A. A., Villanueva, G. L., Vispoel, B., Wagner, G., Yachmenev, A., and Yurchenko, S. N., “The HITRAN2020 Molecular Spectroscopic Database,” *Journal of Quantitative Spectroscopy and Radiative Transfer*, Vol. 277, No. 107949, 2022. <https://doi.org/10.1016/j.jqsrt.2021.107949>.
- [28] Gestion et Etude des Informations Spectroscopiques Atmosphériques, 2011. URL <https://geisa.aeris-data.fr/>, retrieved 01 May 2024.
- [29] SpectralCalc – High-resolution Spectral Modeling, 2009. URL <https://www.spectralcalc.com/info/about>, retrieved 01 May 2024.
- [30] Schreier, F., García, S. G., Hochstaffl, P., and Städt, S., “Py4CAtS—PYthon for Computational ATmospheric Spectroscopy,” *Atmosphere*, Vol. 10, No. 5, 2019, p. 262. <https://doi.org/10.3390/atmos10050262>.
- [31] Serdyuchenko, A., Gorshelev, V., Weber, M., and Burrows, J. P., “New Broadband High-resolution Ozone Absorption Cross-sections,” *Spectroscopy Europe/World*, Vol. 23, No. 6, 2011, pp. 14–17. URL <https://www.spectroscopyeurope.com/article/new-broadband-high-resolution-ozone-absorption-cross-sections>.
- [32] Molecular Spectroscopy Lab at IUP Bremen – Databases, 2011. URL <https://www.iup.uni-bremen.de/gruppen/molspec/databases/referencespectra/o3spectra2011/index.html>, retrieved 01 May 2024.
- [33] Bodhaine, B. A., Wood, N. B., Dutton, E. G., and Slusser, J. R., “On Rayleigh Optical Depth Calculations,” *Journal of Atmospheric and Oceanic Technology*, Vol. 16, No. 11, 1999, pp. 1854–1861. [https://doi.org/10.1175/1520-0426\(1999\)016<1854:ORODC>2.0.CO;2](https://doi.org/10.1175/1520-0426(1999)016<1854:ORODC>2.0.CO;2).